MPC1-like Is a Placental Mammal-specific Mitochondrial Pyruvate Carrier Subunit Expressed in Postmeiotic Male Germ Cells*

Benoît Vanderperre[‡], Kristina Cermakova[‡], Jessica Escoffier[§¶], Mayis Kaba[§¶], Tom Bender[‡], Serge Nef[§¶], and Jean-Claude Martinou[‡1]

From the ‡Department of Cell Biology, the §Swiss Centre for Applied Human Toxicology, and the ¶Department of Genetic Medicine and Development, University of Geneva, 1211 Geneva 4, Switzerland

Selective transport of pyruvate across the inner mitochondrial membrane by the mitochondrial pyruvate carrier (MPC) is a fundamental step that couples cytosolic and mitochondrial metabolism. The recent molecular identification of the MPC complex has revealed two interacting subunits, MPC1 and MPC2. Although in yeast, an additional subunit, MPC3, can functionally replace MPC2, no alternative MPC subunits have been described in higher eukaryotes. Here, we report for the first time the existence of a novel MPC subunit termed MPC1-like (MPC1L), which is present uniquely in placental mammals. MPC1L shares high sequence, structural, and topological homology with MPC1. In addition, we provide several lines of evidence to show that MPC1L is functionally equivalent to MPC1: 1) when co-expressed with MPC2, it rescues pyruvate import in a MPC-deleted yeast strain; 2) in mammalian cells, it can associate with MPC2 to form a functional carrier as assessed by bioluminescence resonance energy transfer; 3) in MPC1 depleted mouse embryonic fibroblasts, MPC1L rescues the loss of pyruvate-driven respiration and stabilizes MPC2 expression; and 4) MPC1- and MPC1L-mediated pyruvate imports show similar efficiency. However, we show that MPC1L has a highly specific expression pattern and is localized almost exclusively in testis and more specifically in postmeiotic spermatids and sperm cells. This is in marked contrast to MPC1/MPC2, which are ubiquitously expressed throughout the organism. To date, the biological importance of this alternative MPC complex during spermatogenesis in placental mammals remains unknown. Nevertheless, these findings open up new avenues for investigating the structure-function relationship within the MPC complex.

The metabolic balance between glycolysis and oxidative phosphorylation (OXPHOS)[2] is of crucial importance in determining cell function and fate. Rapidly proliferating cells rely preferentially on glycolysis despite its lower yield of ATP, because glycolytic intermediates efficiently meet the anabolic needs for sustained cell growth. In rapidly dividing cells, this occurs even in the presence of oxygen, a process called aerobic glycolysis, or the Warburg effect (1, 2). Differentiated cells rely more heavily on OXPHOS to meet the energy demands associated with their specialization. In addition, a shift from glycolytic to oxidative metabolism is necessary for the differentiation process to occur (2–4), and conversely, a hallmark of cancer lies in the rewiring of cellular metabolism toward increased glycolytic flux (5).

Pyruvate, the end product of glycolysis, is imported into the mitochondrial matrix where it fuels the TCA cycle and thereby provides electrons and reducing equivalents to the respiratory chain. Pyruvate-derived acetyl-CoA can also be used as an anabolic substrate for the synthesis of lipids and amino acids. Thus, elucidating the molecular mechanisms that determine the intracellular fate of pyruvate is important for understanding the control of cell metabolism and ultimately of cell function and cell fate. Central to this process is the transport of pyruvate from the cytosol to the mitochondrial matrix.

Cytosolic pyruvate is thought to cross the outer mitochondrial membrane through voltage-dependent anion channel/porin channels (6) and the inner mitochondrial membrane (IMM), through a specific transporter known as the mitochondrial pyruvate carrier (MPC), whose molecular identity has been determined only recently (Refs. 7 and 8; reviewed in Ref. 9). The MPC was found to consist of two highly conserved protein subunits encoded in higher eukaryotes by the genes *MPC1* and *MPC2* (7, 8). MPC1 and MPC2 are small transmembrane proteins of 109 and 127 amino acids, respectively, in humans, which physically interact with each other and form higher molecular weight complexes (8, 10), the full composition of which remains to be fully elucidated.

Because the identification of MPC encoding genes, novel genetic models and molecular tools have flourished to study MPC function. A decrease in MPC activity has been shown to perturb whole body glucose homeostasis through effects on glucose-stimulated insulin secretion (11, 12) and gluconeogenesis (13, 14). In addition, reduced MPC expression (15, 16) and activity (17–19) has been observed in cancer cells, contributing to the Warburg effect. This favors cell growth and metastasis and promotes the establishment and maintenance of the cancer stem cell compartment (15, 16, 20).

² The abbreviations used are: OXPHOS, oxidative phosphorylation; IMM, inner mitochondrial membrane; MPC, mitochondrial pyruvate carrier; BRET, bioluminescence resonance energy transfer; MEF, mouse embryonic fibroblast; LDHA, lactate dehydrogenase A; RNA-seq, RNA-sequencing.

TABLE 1

List of all MPC genes newly identified in this study

The column headings are explained as follows: Official gene symbol, the official gene symbol provided by NCBI, when available; Gene symbol used in this study, the gene symbols used throughout the manuscript, for clarity purposes; Encoded in (accession number), NCBI accession number in which the coding region of the corresponding gene was found by tblastn; REFSEQ protein accession number, provided when available; Paralog of MPC gene (gene symbol), official gene symbol of the paralogous; canonical MPC subunit is indicated for each newly identified gene; Ortholog of human MPC gene (gene symbol), when applicable, the gene symbol of the human ortholog of each newly identified gene is indicated.

Official gene symbol	Gene symbol used in this study	Species	Chromosome	Encoded in (accession number)	REFSEQ protein accession number	Paralog of MPC gene (gene symbol)	Ortholog of human MPC gene (gene symbol)
MPC1L	*MPC1L*	*Homo sapiens*	X	NM_001195522.2	NP_001182451.1	*MPC1*	Not applicable
MPC1L	*MPC1L*	*Bos taurus*	X	NM_001075809.2	NP_001069277.1	*MPC1*	*MPC1L*
MPC1L	*MPC1L*	*Canis lupus*	X	XM_005641252.1	XP_005641309.1	*MPC1*	*MPC1L*
MPC1L	*MPC1L*	*Rattus norvegicus*	X	NM_001109365.1	NP_001102835.1	*MPC1*	*MPC1L*
MPC1L	*MPC1L*	*Felis catus*	X	XM_004000457.2	XP_004000506.1	*MPC1*	*MPC1L*
MPC1L	*MPC1L*	*Ovis aries*	X	XM_004022578.1	XP_004022627.1	*MPC1*	*MPC1L*
MPC1L	*MPC1L*	*Sus scrofa*	X	XM_005673560.2	XP_005673617.1	*MPC1*	*MPC1L*
MPC1L	*MPC1L*	*Heterocephalus glaber*	X	XM_004850018.1	XP_004850075.1	*MPC1*	*MPC1L*
MPC1L	*MPC1L*	*Oryctolagus cuniculus*	X	XM_002719832.2	XP_002719878.1	*MPC1*	*MPC1L*
Gm4984	*MPC1L*	*Mus musculus*	X	NM_001101484.1	NP_001094954.1	*MPC1*	*MPC1L*
Not applicable	*MPC1L*	*Pan troglytes*	X	AC186198.2	not applicable	*MPC1*	*MPC1L*
Gm13570	*MPCLP*	*Mus musculus*	2	XM_006543655.2	XP_006543718.1	*MPC1*	Not applicable
zgc,103678	Not applicable	*Danio rerio*	1	NM_001004662.2	NP_001004662.1	*MPC2*	Not applicable

A detailed characterization of MPC components and how their expression and molecular function is regulated remains incomplete. In prostate cancer cells, the transcription factor COUPTFII inhibits *MPC1* expression favoring tumorigenesis (16), whereas diet-induced obesity and streptozotocin-induced insulin deficiency result in higher expression of MPC subunits (13, 14) and stimulation of pyruvate import (13). It has also been suggested that acetylation of MPC1 decreases pyruvate-driven oxygen consumption in mammalian cells (21). Study of the yeast MPC has revealed a switch in subunit composition depending on growth conditions. In fermentative conditions, the complex is composed of MPC1 and MPC2 (MPC$_{FERM}$), but in oxidative conditions MPC2 is replaced by the yeast specific MPC3 (MPC$_{OX}$), a MPC2 homolog that confers a greater capacity for pyruvate transport (10). In higher eukaryotes, no additional MPC subunits have been described to date.

In an attempt to obtain a more complete picture of the composition of the MPC in higher eukaryotes, we performed a bioinformatics search for additional putative MPC subunits. We discovered a new MPC gene in placental mammals called *MPC1L* (*MPC1-like*). MPC1L does not change pyruvate import efficiency of the MPC, but it is expressed almost exclusively in testis, where it is present only in the postmeiotic germ cells. These cells also show increased expression of MPC2, suggesting an important role for mitochondrial pyruvate import during spermiogenesis and/or for sperm cell function, although the precise role of the variant MPC in these cells has yet to be determined. Our findings demonstrate that the molecular composition of the MPC in placental mammals may be more subtle than was previously anticipated and raise new questions regarding the structure-function relationship within the MPC complex.
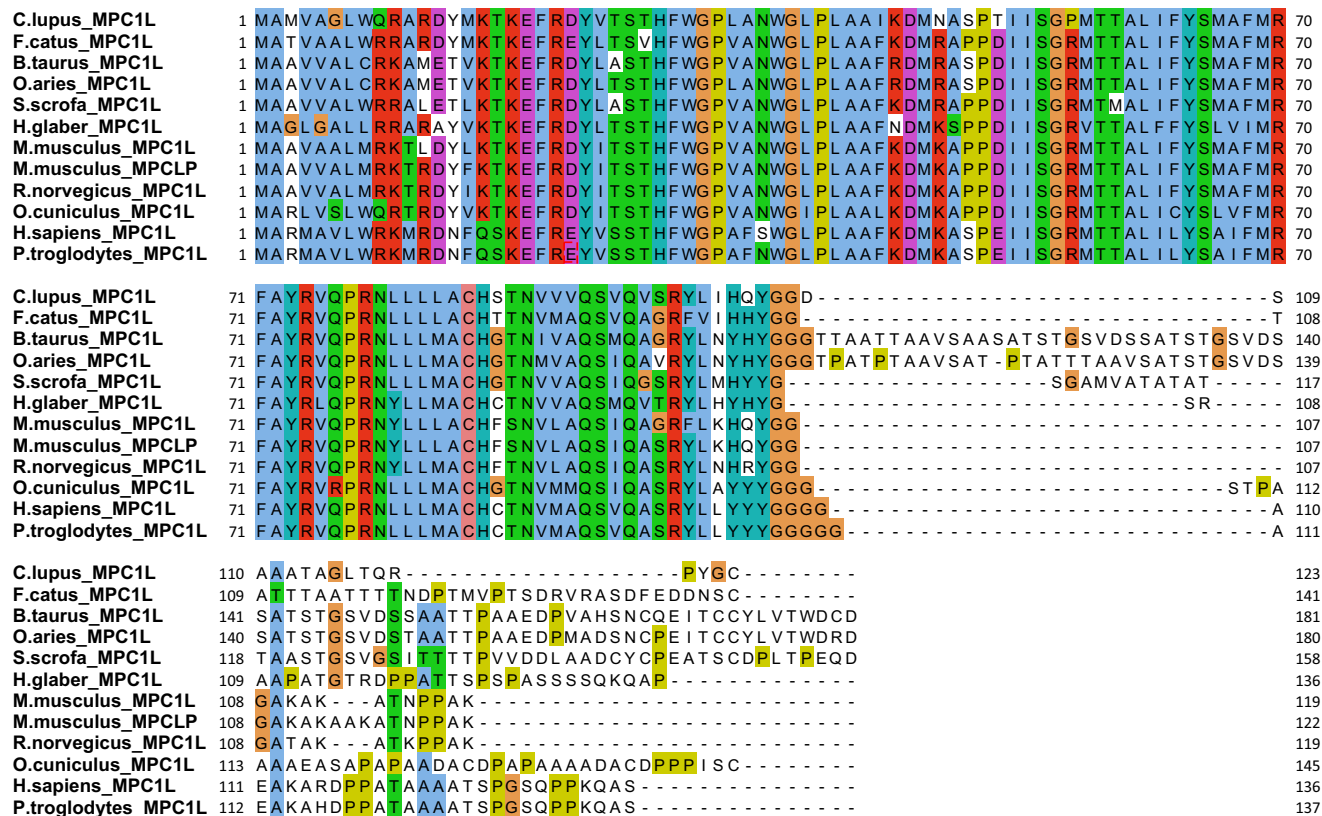
Results

MPC1L (MPC1-like) Is a MPC1 Paralog Specific to Placental Mammals—As part of a search for additional members of the mitochondrial pyruvate carrier (MPC) family, we have used the MPC1 and MPC2 protein sequences from several species as input for an analysis using the tblastn algorithm. This algorithm searches nucleotide databases to identify sequences that encode proteins similar to the input sequence. We identified an *MPC1* paralog, *MPC1L*, on the X chromosome specifically in placental mammals and an additional close homolog of *MPC1L* (MPC-like protein, *Mpclp*) on chromosome 2 of the mouse only. In addition, we identified an *MPC2* paralog in zebrafish, which was not present in any of the other species tested. This gene was not investigated further. As expected, the *MPC3* gene was found in yeast. All new MPC genes identified in this study are listed in Table 1. Multiple sequence alignment revealed a high degree of conservation between *MPC1L* orthologs, with the exception of the C termini, which varied both in length and amino acid composition (Fig. 1*A*). Pairwise alignments between *MPC1* and *MPC1L* in human and mouse also showed strong sequence similarity (Fig. 1, *B* and *C*) except for a slightly extended C terminus in *MPC1L*. In addition, a very high conservation was found between *Mpc1l* and *Mpclp* in mouse (Fig. 1*D*). The RetroGenes track from the UCSC genome browser predicts that *Mpc1l* (and *Mpclp*) from mouse are retrotransposed processed pseudogenes because they contain neither splice sites nor introns found in the parental *Mpc1* gene. Furthermore, no putative ORF could be found by the BESTORF prediction tool. Nevertheless, we were able to identify manually the MPC1L and MPCLP encoding ORFs, and this, together with the strong conservation of MPC1L protein sequence in placental mammals (Fig. 1*A*), strongly suggested to us that the *MPC1L* and *MPCLP* genes encode functional protein products.

MPC1L Is Localized in the IMM and Shows Topological Homology with MPC1—To assess MPC1L subcellular localization, we stably expressed human MPC1L fused to a C-terminal Venus tag (MPC1L-Venus) in HeLa cells. Immunofluorescence experiments showed co-localization of MPC1L-Venus with the mitochondrial protein Tom20 (Fig. 2*A*). This was confirmed by subcellular fractionation experiments, in which MPC1L-Venus was found in the mitochondria enriched fraction together with mitochondrial HSP70, but not in the cytosolic, lactate dehydrogenase A (LDHA)-rich fraction (Fig. 2*B*). MPC1L remained associated with the membrane fraction following alkali treatment (Fig. 2*C*), indicating that it is an integral membrane protein. Furthermore, the proteinase K accessibility assay showed

A

C.lupus_MPC1L	1 MAMVAGLWQRARDYMKTKEFRDYVTSTHFWGPLANWGLPLAAIKDMNASPTIISGPMTTALIFYSMAFMR	70
F.catus_MPC1L	1 MATVAALWRRARDYMKTKEFREYLTSVHFWGPVANWGLPLAAFKDMRAPPDIISGRMTTALIFYSMAFMR	70
B.taurus_MPC1L	1 MAAVVALCRKAMETVKTKEFRDYLASTHFWGPVANWGLPLAAFRDMRASPDIISGRMTTALIFYSMAFMR	70
O.aries_MPC1L	1 MAAVVALCRKAMETVKTKEFRDYLTSTHFWGPLANWGLPLAAFRDMRASPDIISGRMTTALIFYSMAFMR	70
S.scrofa_MPC1L	1 MAAVVALWRRALETLKTKEFRDYLASTHFWGPVANWGLPLAAFKDMRAPPDIISGRMTMALIFYSMAFMR	70
H.glaber_MPC1L	1 MAGLGALLRRARAYVKTKEFRDYLTSTHFWGPVANWGLPLAAFNDMKSPPDIISGRVTTALFFYSLVIMR	70
M.musculus_MPC1L	1 MAAVAALMRKTLDYLKTKEFRDYITSTHFWGPVANWGLPLAAFKDMKAPPDIISGRMTTALIFYSMAFMR	70
M.musculus_MPCLP	1 MAAVVALMRKTRDYFKTKEFRDYITSTHFWGPVANWGLPLAAFKDMKAPPDIISGRMTTALIFYSMAFMR	70
R.norvegicus_MPC1L	1 MAAVVALMRKTRDYIKTKEFRDYITSTHFWGPVANWGLPLAAFKDMKAPPDIISGRMTTALIFYSMAFMR	70
O.cuniculus_MPC1L	1 MARLVSLWQRTRDYVKTKEFRDYITSTHFWGPVANWGIPLAALKDMKAPPDIISGRMTTALICYSLVFMR	70
H.sapiens_MPC1L	1 MARMAVLWRKMRDNFQSKEFREYVSSTHFWGPAFSWGLPLAAFKDMKASPEIISGRMTTALILYSAIFMR	70
P.troglodytes_MPC1L	1 MARMAVLWRKMRDNFQSKEFREYVSSTHFWGPAFNWGLPLAAFKDMKASPEIISGRMTTALILYSAIFMR	70

C.lupus_MPC1L	71 FAYRVQPRNLLLLACHSTNVVVQSVQVSRYLIHQYGGD------------------------------------S	109
F.catus_MPC1L	71 FAYRVQPRNLLLLACHTTNVMAQSVQAGRFVIHHYGG-------------------------------------T	108
B.taurus_MPC1L	71 FAYRVQPRNLLLMACHGTNIVAQSMQAGRYLNYHYGGGTTAATTAAVSAASATSTGSVDSSATSTGSVDS	140
O.aries_MPC1L	71 FAYRVQPRNLLLMACHGTNMVAQSIQAVRYLNYHYGGGTPATPTAAVSAT-PTATTTAAVSATSTGSVDS	139
S.scrofa_MPC1L	71 FAYRVQPRNLLLMACHGTNVVAQSIQGSRYLMHYYG----------------SGAMVATATAT-----	117
H.glaber_MPC1L	71 FAYRLQPRNYLLMACHCTNVVAQSMQVTRYLHYHYG-----------------------------------SR-----	108
M.musculus_MPC1L	71 FAYRVQPRNYLLLACHFSNVLAQSIQAGRFLKHQYGG-------------------------------------	107
M.musculus_MPCLP	71 FAYRVQPRNYLLLACHFSNVLAQSIQASRYLKHQYGG-------------------------------------	107
R.norvegicus_MPC1L	71 FAYRVQPRNYLLMACHFTNVLAQSIQASRYLNHRYGG-------------------------------------	107
O.cuniculus_MPC1L	71 FAYRVRPRNLLLMACHGTNVMMQSIQASRYLAYYYGGG-----------------------------------STPA	112
H.sapiens_MPC1L	71 FAYRVQPRNLLLMACHCTNVMAQSVQASRYLLYYYGGGG-----------------------------------A	110
P.troglodytes_MPC1L	71 FAYRVQPRNLLLMACHCTNVMAQSVQASRYLLYYYGGGGG-----------------------------------A	111

C.lupus_MPC1L	110 AAATAGLTQR------------------PYGC---------	123
F.catus_MPC1L	109 ATTTAATTTTNDPTMVPTSDRVRASDFEDDNSC-------	141
B.taurus_MPC1L	141 SATSTGSVDSSAATTPAAEDPVAHSNCQEITCCYLVTWDCD	181
O.aries_MPC1L	140 SATSTGSVDSTAATTPAAEDPMADSNCPEITCCYLVTWDRD	180
S.scrofa_MPC1L	118 TAASTGSVGSITTTTPVVDDLAADCYCPEATSCDPLTPEQD	158
H.glaber_MPC1L	109 AAPATGTRDPPATTSPSPASSSSQKQAP-------------	136
M.musculus_MPC1L	108 GAKAK---ATNPPAK-------------------------	119
M.musculus_MPCLP	108 GAKAKAAKATNPPAK-------------------------	122
R.norvegicus_MPC1L	108 GATAK---ATKPPAK-------------------------	119
O.cuniculus_MPC1L	113 AAAEASAPAPAADACDPAPAAAADACDPPPISC-------	145
H.sapiens_MPC1L	111 EAKARDPPATAAAATSPGSQPPKQAS---------------	136
P.troglodytes_MPC1L	112 EAKAHDPPATAAAATSPGSQPPKQAS---------------	137

B

hMPC1	1 ---MAGALVRKAADYVRSKDFRDYLMSTHFWGPVANWGLPIAAINDMKKSPEIISGRMTFALCCYSLTFMR	68
hMPC1L	1 MARMA-VLWRKMRDNFQSKEFREYVSSTHFWGPAFSWGLPLAAFKDMKASPEIISGRMTTALILYSAIFMR	70

hMPC1	69 FAYKVQPRNWLLFACHATNEVAQLIQGGRLIKH-----------EMTKTASA-------------	109
hMPC1L	71 FAYRVQPRNLLLMACHCTNVMAQSVQASRYLLYYYGGGGAEAKARDPPATAAAATSPGSQPPKQAS	136

<center>identity (%): 48.2   similarity (%): 57.7</center>

C

mMPC1	1 ---MAGALVRKAADYVRSKDFRDYLMSTHFWGPVANWGLPIAAINDMKKSPEIISGRMTFALCCYSLTFMR	68
mMPC1L	1 MAAVAALMRKTLDYLKTKEFRDYITSTHFWGPVANWGLPLAAFKDMKAPPDIISGRMTTALIFYSMAFMR	70

mMPC1	69 FAYKVQPRNWLLFACHVTNEVAQLIQGGRLINYEMSKRPSA--------	109
mMPC1L	71 FAYRVQPRNYLLLACHFSNVLAQSIQAGRFLKHQYGGGAKAKATNPPAK	119

<center>identity (%): 55.5   similarity (%): 68.9</center>

D

mMPC1L	1 MAAVAALMRKTLDYLKTKEFRDYITSTHFWGPVANWGLPLAAFKDMKAPPDIISGRMTTALIFYSMAFMR	70
mMPCLP	1 MAAVVALMRKTRDYFKTKEFRDYITSTHFWGPVANWGLPLAAFKDMKAPPDIISGRMTTALIFYSMAFMR	70

mMPC1L	71 FAYRVQPRNYLLLACHFSNVLAQSIQAGRFLKHQYGGGAK---AKATNPPAK	119
mMPCLP	71 FAYRVQPRNYLLLACHFSNVLAQSIQASRYLKHQYGGGAKAKAAKATNPPAK	122

<center>identity (%): 93.4   similarity (%): 94.3</center>
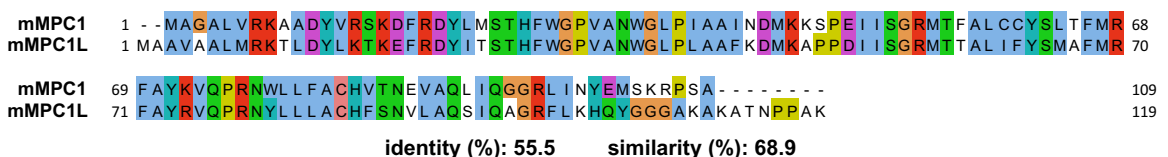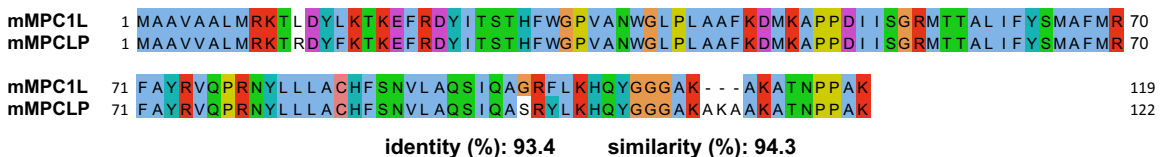
FIGURE 1. **Sequence alignments between MPC1 family members.** *A*, multiple sequence alignments of MPC1L protein sequence from the indicated species. MPCLP from mouse is also included in the comparison. The high conservation and alignment quality seen in the first 100 amino acids suggest a conserved functionality. *B–D*, human MPC1 and MPC1L (*B*), mouse MPC1 and MPC1L (*C*), and mouse MPC1L (*D*) and the mouse-specific subunit MPCLP. The percentage of identity and similarity are indicated beneath each alignment. *A–D*, the Clustal X color scheme was used.

that MPC1L is degraded only after swelling and rupture of the outer membrane (Fig. 2*D*). These results indicate that MPC1L is an integral IMM protein, as was previously shown for MPC1 (7).

In *Saccharomyces cerevisiae*, MPC1 is inserted in the IMM via two transmembrane segments, whereas the functionally redundant MPC2 and MPC3 subunits possess three transmembrane segments (10). We reasoned that a topological similarity between MPC1 and MPC1L in placental mammals would suggest a functional similarity between these two proteins. We therefore performed *in silico* prediction of transmembrane segments by applying two different prediction methods to the protein sequences of human MPC1, MPC1L and MPC2 (data not shown). The TopPred algorithm identified two transmembrane domains in both MPC1 and MPC1L and three in MPC2. The TMHMM algorithm also identified two transmembrane seg-
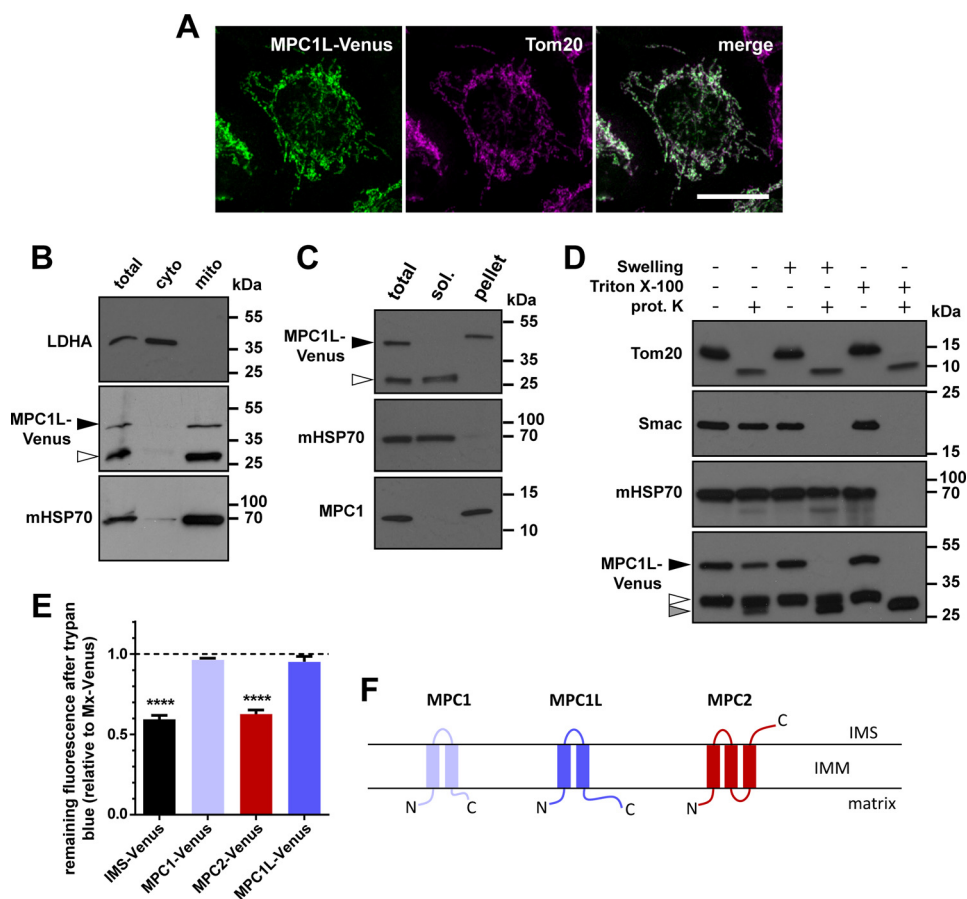
FIGURE 2. **MPC1L is located in the inner mitochondrial membrane and shares topological homology with MPC1.** *A*, immunofluorescence study in HeLa cells showing co-localization of the human MPC1L-Venus (MPC1L-Venus) fusion protein and the endogenous mitochondrial marker, Tom20. *B*, the cells shown in *A* were submitted to subcellular fractionation, and the results of Western blotting show enrichment of MPC1L-Venus in the mitochondrial (*mito*, mHSP70-rich) fraction, but not in the cytosolic (*cyto*, LDHA-rich) fraction. *Black arrowhead*, full-length MPC1L-Venus; *white arrowhead*, Venus-containing fragment resistant to endogenous degradation. *C*, alkali treatment of the mitochondria-rich fraction shown in *B* followed by ultracentrifugation and Western blotting reveals that MPC1L-Venus, similar to MPC1, is an integral membrane protein (pellet), whereas the mitochondrial matrix protein HSP70 is found in the soluble fraction (*sol.*). Note that the C-terminal Venus-containing fragment is soluble (*white arrowhead*). *D*, proteinase K (*prot. K*) accessibility assay in which the mitochondria-rich fraction from HeLa cells expressing MPC1L-Venus was treated as indicated. Each sample was then subjected to SDS-PAGE and Western blotting using antibodies directed against Tom20 (outer mitochondrial membrane), Smac (intermembrane space), mHSP70 (matrix), and Venus. The full-length MPC1L-Venus (*black arrowhead*) is fully sensitized to digestion only after swelling of the outer membrane, indicating its localization in the inner membrane, whereas the soluble Venus-containing fragment (*white arrowhead*) accumulates in the matrix because it becomes accessible to proteinase K only upon treatment with detergent. The Venus tag appears resistant to full proteolytic digestion even in the presence of Triton X-100 (*gray arrowhead*). Note that after digestion, residual MPC1L-Venus fragments can only be detected by the anti-Venus antibody if they contain the C-terminal, Venus-fused region. *E*, Trypan blue quenching experiment performed on HeLa cells stably expressing the indicated constructs. The fluorescence remaining after quenching by trypan blue is shown relative to Matrix-Venus (Mx-Venus) indicated by the *dashed line*. ****, $p < 0.0001$, one-way analysis of variance. The pronounced quenching of the fluorescence compared with Mx-Venus indicates accessibility of the C-terminal Venus to the intermembrane space (*IMS*). $n \geq 3$ cells were quantified per experiment, and results are from three independent experiments. The data are means ± S.E. *F*, model of MPC1, MPC1L, and MPC2 transmembrane topology based on our results.

ments in MPC1L, but for MPC1 and MPC2, the posterior probabilities (22) for the putative transmembrane segments did not pass the TMHMM threshold (data not shown). Nevertheless, posterior probabilities were elevated in these regions, fully compatible with the results from TopPred. We tested these predictions experimentally using an assay that relies on the observation that the fluorescence of C-terminal Venus fusion proteins is quenched in the presence of trypan blue (23, 24). In live, digitonin-permeabilized cells, trypan blue can cross the outer mitochondrial membrane but not the digitonin-insensitive IMM. The decrease in fluorescence intensity for a given construct thus reflects the accessibility of the C-terminal Venus tag to trypan blue, providing insight into the topological orientation of transmembrane proteins. In control experiments we

compared constructs in which Venus was localized either in the mitochondrial matrix (Mx-Venus) or in the intermembrane space (IMS-Venus). As shown in Fig. 2*E*, IMS-Venus was strongly quenched compared with Mx-Venus, showing that the assay performed as expected. Analysis using the MPC constructs showed that the MPC2-Venus fluorescence was quenched to the same extent as IMS-Venus, indicating that the C terminus of MPC2 is exposed to the IMS. In contrast, both MPC1-Venus and MPC1L-Venus behaved like Mx-Venus, indicating that their C termini are present on the matrix side of the IMM (Fig. 2*E*). Based on these results, our model of the topology of human MPC subunits is summarized in Fig. 2*F*. The model is in accordance with the previously published topological analysis of MPC subunits in budding yeast

(10). Together, our data indicate that MPC1L is inserted in the IMM, where it shares structural and topological similarity with MPC1.

MPC1L Can Replace MPC1 to Form a Functional MPC—To determine whether MPC1L is a functional MPC subunit, we used a complementation assay in a yeast strain lacking all MPC subunits ($mpc1\Delta/mpc2\Delta/mpc3\Delta$). This strain fails to grow on synthetic medium lacking branched chain amino acids, for which mitochondrial pyruvate is an essential precursor in yeast (7, 8, 10). It was shown previously that this growth defect can be rescued by co-expression of the mouse MPC1 and MPC2 orthologs (7), and we have confirmed these results using human MPC1 and MPC2 (Fig. 3A). Furthermore, whereas expression of neither human MPC1L nor MPC2 alone was sufficient to rescue growth of the MPC lacking yeast, co-expression of MPC1L and MPC2 restored cell growth to a level similar to that seen following co-expression of MPC1 and MPC2. We conclude that MPC1L can substitute for MPC1 to form a functional MPC complex.

To confirm that MPC1L associates physically with MPC2, we took advantage of the bioluminescence resonance energy transfer (BRET) assay that we have recently developed to monitor the activity of the MPC in real time (17). In the earlier study, either MPC1 or MPC2 (from human origin) was fused to a BRET donor (*Renilla* luciferase, RLuc8), and co-expressed with the corresponding complementary subunit fused to Venus, the BRET acceptor. In both configurations, a specific BRET signal was observed, indicative of heteromerization between MPC1 and MPC2. Homomerization of MPC2, but not of MPC1, was also observed. To study the activity of MPC1L, we first generated the MPC1L-RLuc8 fusion construct as the donor molecule. In co-expression studies, an increase in the BRET signal could be observed only in the presence of MPC2-Venus, but not in the presence of MPC1L-Venus or the empty vector (Fig. 3B, *left panel*). In the complementary experiment, MPC2-RLuc8 was used as a donor, and the increase in BRET was obtained when either MPC1-Venus or MPC1L-Venus was co-expressed as the acceptor (Fig. 3B, *right panel*). The BRET signal indicates close proximity of the C-terminal tags and thus demonstrates that MPC1L is able to interact physically with MPC2.

To study the functionality of the MPC1L/MPC2 complex, we have followed the changes in the BRET signal in the presence of pyruvate. We concluded previously that binding of pyruvate to the MPC followed by pyruvate transport across the IMM leads to conformational changes in the MPC1/MPC2 heteromers, which result in a change in BRET intensity and which allow us to monitor the pyruvate import activity of the MPC in real time (17). To determine the activity of the MPC1L/MPC2 heteromers in this assay, we performed time course experiments using cells co-transfected with MPC1L-RLuc8/MPC2-Venus, MPC2-RLuc8/MPC1L-Venus, or the positive control plasmids MPC2-RLuc8/MPC1-Venus (Fig. 3C). For each combination, addition of pyruvate elicited a rapid and stable increase in BRET relative to the PBS control. Thus, the BRET data for the MPC1L/MPC2 complex in the presence of pyruvate further indicate that this complex, similar to the canonical MPC1/MPC2 complex, is competent for pyruvate import.

To confirm that MPC1L can sustain pyruvate import into mammalian mitochondria, we took advantage of previously described MPC-deficient mouse embryonic fibroblasts (MEFs) in which MPC1 expression had been ablated using a gene trap strategy (17, 25). These cells display no detectable MPC1 by Western blotting analysis (Fig. 3D). Furthermore, the MPC2 protein was also undetectable, despite the presence of its mRNA (25), presumably because MPC2 is degraded in the absence of MPC1. Interestingly, Western blots using our in-house antibody against the C terminus of mouse MPC1L, showed no compensatory expression of the endogenous MPC1L protein in the mitochondria-rich fraction from these cells (Fig. 3D). Because, as we showed previously, the *Mpc1* KO MEFs display no residual mitochondrial pyruvate import activity (25), they provide an useful platform to evaluate the function of MPC1L. Rescued cell lines were generated from the parental *Mpc1* KO MEFs by lentiviral transduction with C-terminally FLAG-tagged MPC1, MPC1L, or MPCLP or with a GFP negative control. All FLAG-tagged constructs were expressed at comparable levels as assessed by Western blotting and stable constitutive expression of MPC1, MPC1L, or MPCLP, but not GFP, was found to rescue MPC2 expression (Fig. 3D), suggesting that in these cells, stable MPC2-containing MPC complexes were formed. To assess the functionality of the MPC1L- or MPCLP-containing MPC complexes, we performed respirometry experiments on permeabilized cells using a Seahorse flux analyzer. *Mpc1* KO and GFP-rescued cells showed a basal level of pyruvate-driven carbonyl cyanide-4-(trifluoromethoxy)phenylhydrazone-stimulated oxygen consumption rates, whereas this parameter was significantly increased following expression of MPC1, MPC1L, or MPCLP (Fig. 3, E and F). Taken together, the data presented in Fig. 3 demonstrate that the protein products from the MPC1L and MPCLP genes are able to interact dynamically with MPC2 to form fully functional MPC complexes capable of driving mitochondrial pyruvate import.

MPC1- and MPC1L-containing MPCs Display Similar Pyruvate Import Efficiency—We next asked whether the physiological relevance for the existence of alternative MPC complexes in placental mammals lies in possible differences in pyruvate import efficiency, similar to that reported in yeast (10). The respirometry experiments shown in Fig. 3 (E and F) were performed in the presence of excess pyruvate (10 mM), far exceeding the physiological pyruvate concentration in the cytosol (10–100 μM) (26, 27), which could mask some possible differences in pyruvate import efficiency of the alternative MPC complexes. To compare the relative efficiency of pyruvate import in the MPC1 or MPC1L rescued MEFs, we conducted a respirometry experiment in the presence of increasing concentrations of pyruvate (Fig. 4A). At all concentrations of pyruvate, the carbonyl cyanide-4-(trifluoromethoxy)phenylhydrazone-driven respiration was similar between the two rescued cell lines. In a further experiment, we measured the pyruvate decarboxylation rate in the parental MPC1 KO MEFs, compared with the GFP-, MPC1-, MPC1L-, and MPCLP-rescued cells, reasoning that differences in pyruvate import efficiency would be reflected in the levels of mitochondrial pyruvate-derived CO_2 after decarboxylation to acetyl-CoA by pyruvate dehydrogenase. We therefore quantified the $^{14}CO_2$ released after import

A

B

C

D

E

F
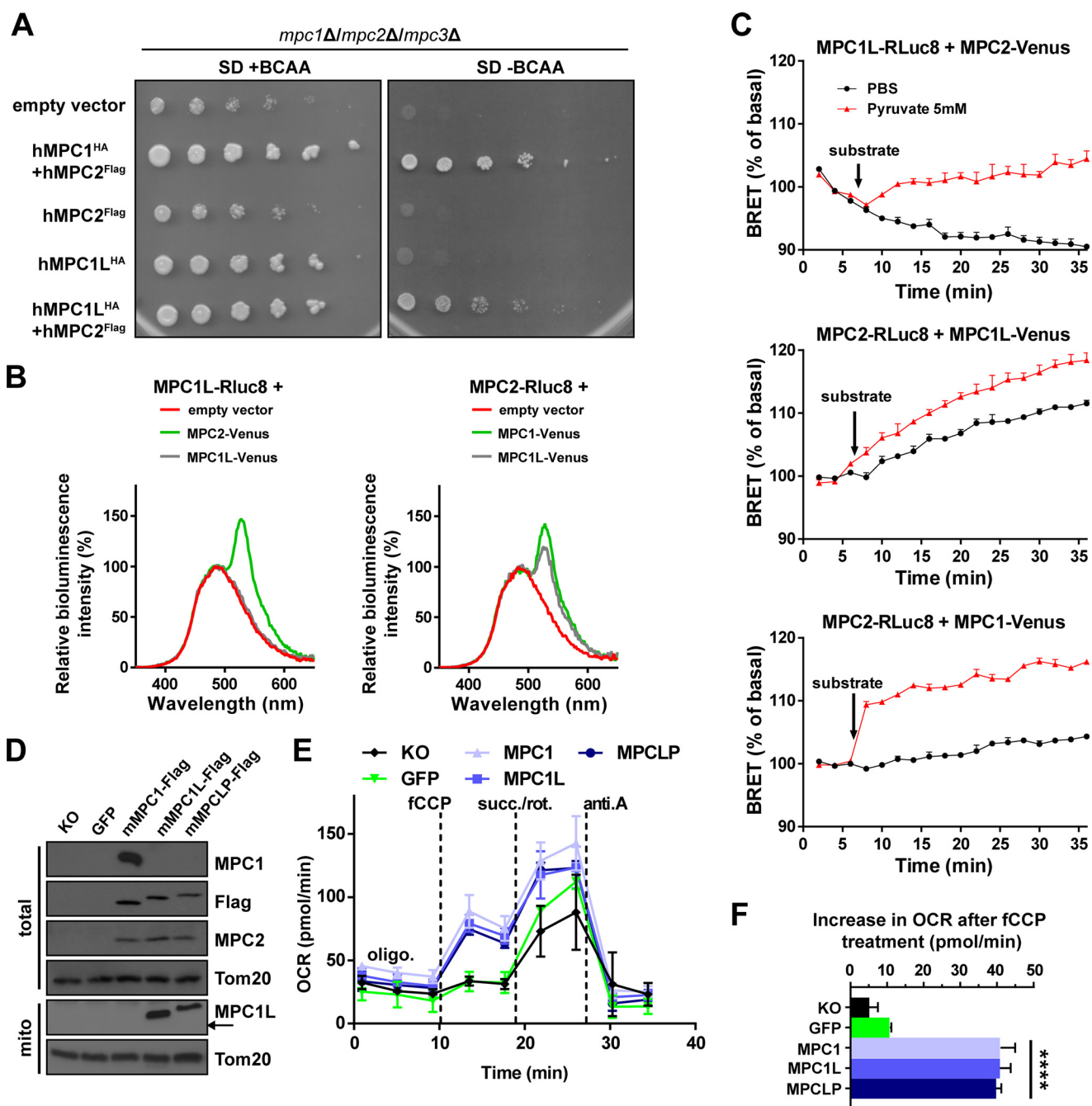
FIGURE 3. **MPC1L is a functional homolog of MPC1.** *A*, spot assay using *mpc1Δ/mpc2Δ/mpc3Δ* yeast cells transformed with expression plasmids containing the indicated constructs, and grown on medium containing (+*BCAA*) or lacking (−*BCAA*) branched chain amino acids. *B*, HEK293T cells were co-transfected with the indicated constructs. After 48 h, cells were incubated with the coelenterazine h substrate for the bioluminescent RLuc8 protein, and the luminescence intensity was recorded in spectral scanning mode (350–650 nm). Relative luminescence intensities compared with the values obtained for the RLuc8 fusion protein expressed alone are indicated. *C*, time course of BRET signal (percentage of basal BRET) in HEK293T cells co-transfected with the indicated BRET donor/acceptor pairs and stimulated at the times indicated (vertical arrows) with PBS (vehicle) or pyruvate. The data are means ± S.E., *n* = 3 with three technical replicates per condition per experiment. *D*, Western blotting analysis of the total and mitochondria-enriched fractions (*mito*) from parental MPC1 KO MEFs either alone or following rescue with mMPC1-FLAG, mMPC1L-FLAG, mMPCLP-FLAG, or GFP. Western blots were probed using the antibodies indicated. The *arrow* indicates the theoretical size of untagged MPC1L. *E*, representative profiles of oxygen consumption rates (*OCR*) in the XF-PMP permeabilized cell lines indicated, in the presence of pyruvate/malate (10 mM/1 mM) as carbon sources. The following compounds were injected at the times indicated by *dashed lines*. *fCCP*, carbonyl cyanide-4-(trifluoromethoxy)phenylhydrazone (2 μM); *succ./rot.*, succinate/rotenone, 10 mM/1 μM; *anti. A*, antimycin A, 1 μM. All measurements were done in the presence of oligomycin (*oligo.*, 1 μM) to inhibit ATP-linked respiration. The data are means ± S.D., *n* = 3. *F*, absolute increase in oxygen consumption rate after addition of carbonyl cyanide-4-(trifluoromethoxy)phenylhydrazone relative to oligomycin condition observed in *E*; the data are means ± S.E.; *n* = 3. ****, *p* < 0.0001 (one-way analysis of variance).

of 1-[¹⁴C]pyruvate and decarboxylation by pyruvate dehydrogenase, and we observed that MPC1L- and MPCLP-expressing cells displayed pyruvate decarboxylation rates that were indistinguishable from the values obtained using the MPC1-ex-

pressing cells (Fig. 4*B*). All three cell lines exhibited pyruvate decarboxylation rates that were well in excess of the basal rates seen in the MPC1 KO and GFP-rescued cells. In conclusion, these results indicate that no difference in mitochondrial pyru-
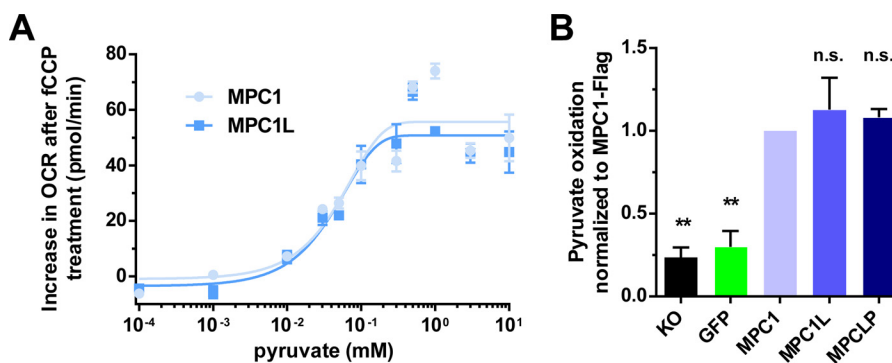
FIGURE 4. **MPC1 and MPC1L have similar pyruvate import efficiencies.** *A*, absolute increase in oxygen consumption rates (*OCR*) after carbonyl cyanide-4-(trifluoromethoxy)phenylhydrazone (*fCCP*; 2 μM) treatment relative to oligomycin (1 μM) condition in MPC1 KO MEFs rescued with mMPC1-FLAG (MPC1) or mMPC1L-FLAG (MPC1L), with pyruvate (increasing concentrations) and malate provided as carbon sources. The data are means $\pm$ S.E. *B*, pyruvate oxidation rates in either the parental MPC1 KO MEFs or in cells rescue with mMPC1-FLAG, mMPC1L-FLAG, mMPCLP-FLAG, or GFP. The data are means $\pm$ S.E., $n = 3$. **, $p < 0.001$; *n.s.*, not significant; one-way analysis of variance compared with the MPC1 rescued condition.

vate import activity exists between different MPC complexes from placental mammals.

MPC1L and MPCLP Are Specifically Expressed in Adult Reproductive Tissues—To investigate whether alternative MPC complexes could have different tissue expression patterns, we took advantage of previously published and publicly available proteomics analyses. An overview of the relative expression levels of MPC1, MPC1L, and MPC2 in several fetal and adult tissues and cells types from human origin was obtained using the Human Proteome Map repository (28). As previously shown, MPC1 and MPC2 expression is ubiquitous and especially high in adult heart, liver, and kidney (Fig. 5*A*). On the other hand, MPC1L was found only in fetal heart and adult gonads, with the most prominent expression being observed in testis. The second data set we interrogated contains the mitochondrial proteomics data from 14 different mouse tissues (29). This data set confirmed the ubiquitous expression of MPC1 and MPC2 and revealed that despite the high levels of MPC2 in testis mitochondria, this tissue showed the lowest abundance of MPC1 (Fig. 5*B*). Fully consistent with our first analysis, this correlated with high testis-specific expression of MPC1L and MPCLP, both of which could be distinguished by unique peptides (Fig. 5*C*) despite their high sequence similarity (Fig. 1*D*). Western blotting analysis of various mouse tissues essentially confirmed the ubiquitous expression of MPC1 and MPC2 (Fig. 5*D*), whereas MPC1L was detected only in testis and in a sperm cell lysate, but not in ovary, pointing to a specific function of this alternative MPC subunit in testis, possibly in male gametes.

In Testis, MPC1L Is Expressed in Haploid Germ Cells—To obtain further insight into the possible physiological relevance of the testis-specific expression of the alternative MPC complex, we extended our investigation to a more detailed analysis of testicular cells types. We first used a previously published RNA-sequencing (RNA-seq) data set from mouse germ cells at different stages of spermatogenesis (30). The relative mRNA expression level for *Mpc1*, *Mpc1l* and *Mpc2* in germ cells at the indicated stage of spermatogenesis is shown in Fig. 6*A* (no data were available for *Mpclp*). The level of *Mpc1* expression appears to remain quite stable throughout spermatogenesis, although a progressive decrease from diploid preleptotene spermatocytes

toward haploid spermatids was observed. Intriguingly, *Mpc1l* expression was restricted exclusively to the round and elongated haploid spermatids, as they undergo differentiation toward mature sperm cells (spermiogenesis). *Mpc2* expression was ubiquitous, and particularly prominent in spermatids, suggesting that a progressive increase in total level of MPC complexes occurs during spermiogenesis.

Immunofluorescence results using mouse testis cryosections confirmed the RNA-seq data (Fig. 6*A*). All cell types stained positively for MPC1 and MPC2 (Fig. 6, *B* and *C*), including the differentiating sperm cells, which possess a mitochondria-rich mid-piece. In contrast, MPC1L was expressed at very high levels in the mid-piece of sperm cells, whereas expression in round spermatids (see DAPI staining, round nuclei with a large heterochromatic chromocenter) (31) was only seen following longer exposure (Figs. 6, *D* and *E*, and 7*B*). This was confirmed by a co-staining with the acrosomal matrix protein SP56 (32), because cells containing a premature acrosome as well as a heterochromatic chromocenter were positive for MPC1L staining (Fig. 6*F*). Spermatocytes (synaptonemal complex protein 3 (Sycp3)-positive cells) and other cell types apart from spermatids and sperm cells were all MPC1L-negative, in full agreement with the RNA-seq data (Fig. 6*A*). The increasing levels of MPC1L observed during spermiogenesis were not a result of an overall increase in mitochondrial protein content, because spermatids and sperm cells were not particularly enriched for either the outer membrane protein Tom20 or the inner membrane protein Cox IV (Fig. 7, *A* and *B*). Co-localization between Cox IV and MPC1L confirmed the mitochondrial localization of MPC1L in round spermatids (Fig. 7*B*), as well as in the mid-piece of sperm cells (Fig. 7*C*).

Discussion

The present study describes for the first time a placental mammal-specific alternative MPC1 subunit of the mitochondrial pyruvate carrier, termed MPC1-like (MPC1L). Our results demonstrate a preferred expression of MPC1L during spermiogenesis (Fig. 6), whereas mass spectrometry data indicate some expression of MPC1L in human fetal heart and adult ovary (Fig. 5), although this awaits further confirmation. Indeed, the current version of the EMBL Expression Atlas
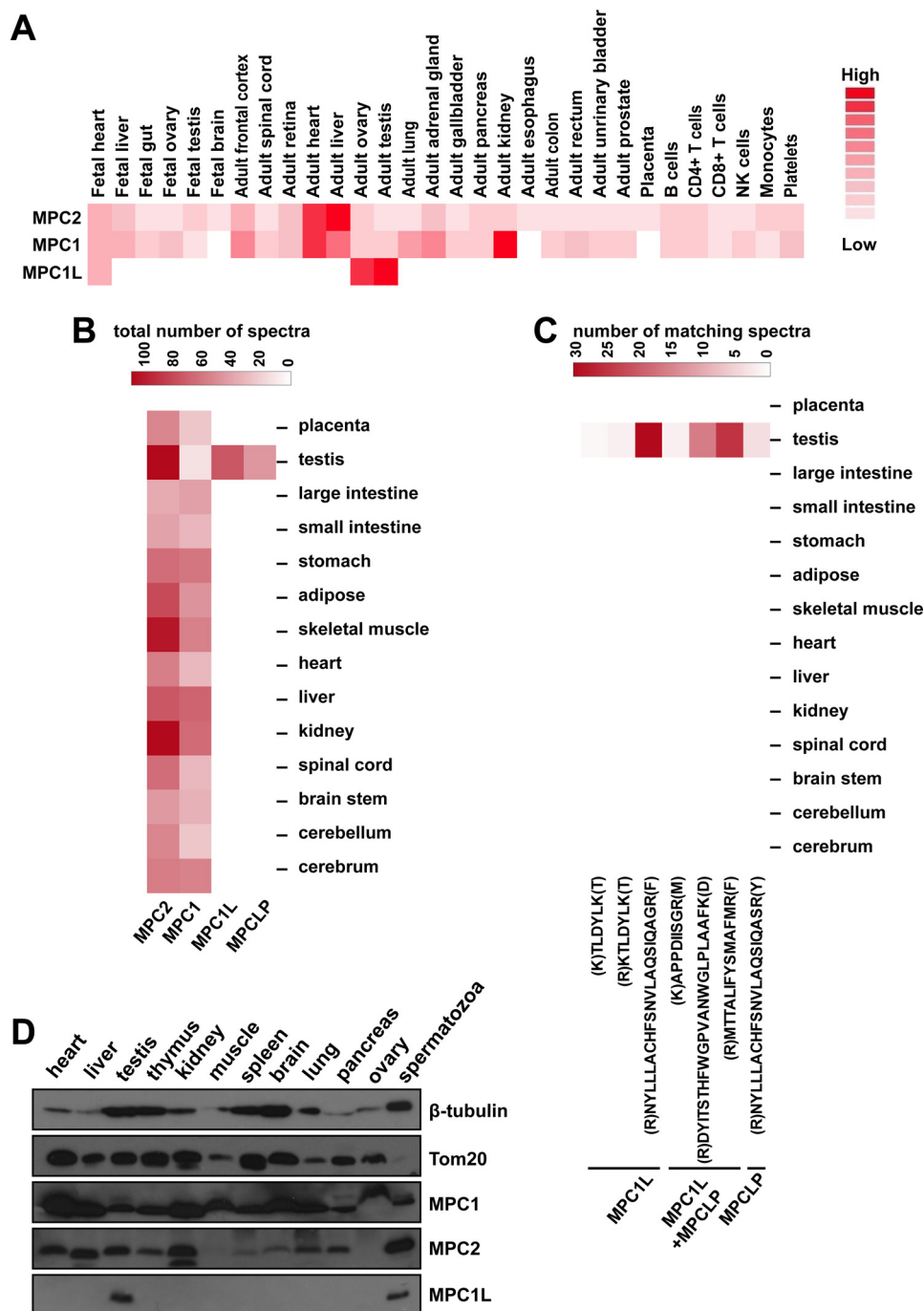
FIGURE 5. **Comparative tissue expression pattern of MPC1, MPC1L, and MPC2 in human and mouse.** *A*, expression patterns of MPC1, MPC1L, and MPC2 in fetal and adult human tissues and cell types, based on mass spectrometry data from the Human Proteome Map repository (28). *B*, expression patterns of MPC1, MPC1L, MPCLP, and MPC2 in mitochondria from 14 different mouse tissues, based on the mass spectrometry data used for the Mitocarta project (29). *C*, peptide evidence for the expression of MPC1L and MPCLP in mouse testis mitochondria. Heat map showing unique peptides for MPC1L (3 peptides) or MPCLP (1 peptide), as well as shared peptides (3), detected by MS/MS in the tissues indicated (data from Ref. 29). The peptide sequences (with flanking residues in *parentheses*) are indicated, and for each peptide, the number of matching spectra is represented by the color code. *D*, MPC1, MPC1L, and MPC2 expression was analyzed by Western blotting in the indicated mouse tissues and in sperm cells.

reports no expression of the *MPC1L* gene in human ovary. We cannot exclude that expression of this alternate MPC subunit might occur in other tissues under particular physiological and pathological conditions. Thus, this discovery should be taken into account in future studies focusing on MPC function in placental mammals.

In yeast, two alternative complexes have been described that accommodate MPC efficiency to cellular metabolism (10). In contrast, the two alternative MPC complexes from placental mammals have similar pyruvate import activities (Fig. 4), which is well supported by the fact that the two alternative subunits, MPC1 and MPC1L, are similar in amino acid sequence (Fig. 1, *B* and *C*), membrane topology (Fig. 2) and in their ability to form a functional complex with MPC2 (Fig. 3). We suggest that this additional carrier may allow better spatiotemporal regulation of MPC function, which might have functional implications
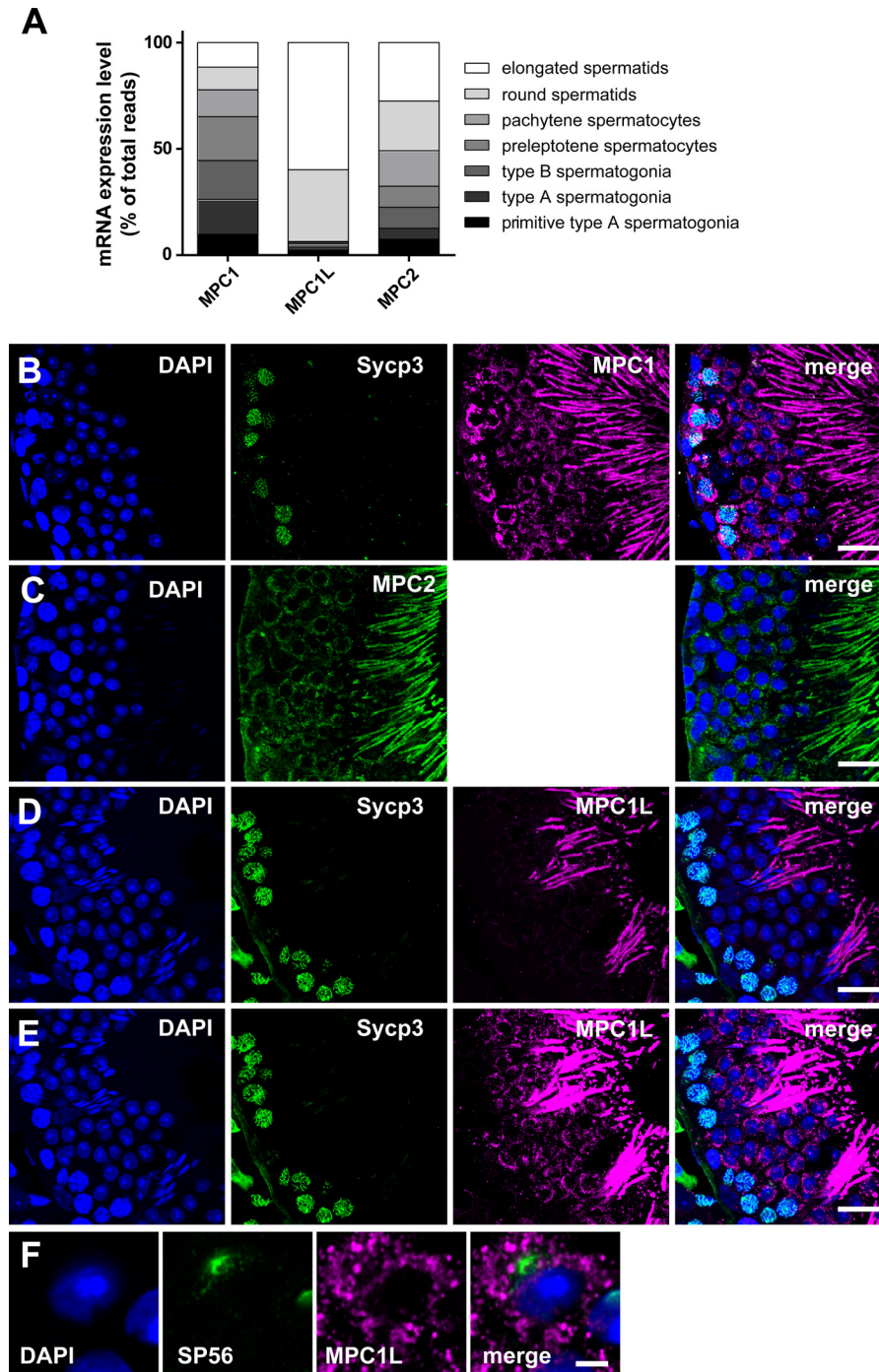
FIGURE 6. **MPC1L is expressed in postmeiotic germ cells from mouse testis.** *A*, expression of *Mpc1*, *Mpc1l*, and *Mpc2* mRNAs in the indicated spermatogenic cell types from mouse testis as assessed by RNA-seq data in Gan *et al.* (30). *B–F*, cryosections through seminiferous tubules from mouse testis showing the early spermatocytes on the *left* of the image, and the round and elongating postmeiotic spermatids on the *right* of the image toward the lumen. The nuclei were stained with DAPI, and immunofluorescent studies were performed using antibodies as follows: MPC1 and the Sycp3 (synaptonemal complex protein 3), which is located between homologous chromosomes during meiotic prophase (*B*), and MPC2 (*C*). *D* and *E*, Sycp3 and MPC1L with low (*D*) and high (*E*) MPC1L exposure times showing specific expression of MPC1L in spermatids and the mid-piece of sperm cells. *F*, MPC1L and the acrosomal marker SP56 (sperm protein 56) in a round spermatid. *B–E*, *scale bar*, 20 μm. *F*, a round spermatid is shown at higher magnification. *Scale bar*, 2.5 μm.

during spermatogenesis or for sperm cell function, but clarification of its role will require further experimentation.

The transcriptome of germ cells varies greatly during the course of spermatogenesis (30, 33), indicating that transcriptional regulation is crucial for spermatogenesis to ensure the availability of appropriate precursor pools, progression of meiosis, and differentiation of haploid cells into fully mature sper-matozoa. As part of this process, MPC1L and MPC2 levels increase during spermiogenesis (Fig. 6), indicating that a high expression of the MPC might be of major importance for sperm cell differentiation and/or function. We speculate that the rather constant MPC1 expression levels in the germ cell lineage during spermatogenesis (Fig. 6) might not be sufficient to meet the demand in MPC subunits, at least in placental mammals.
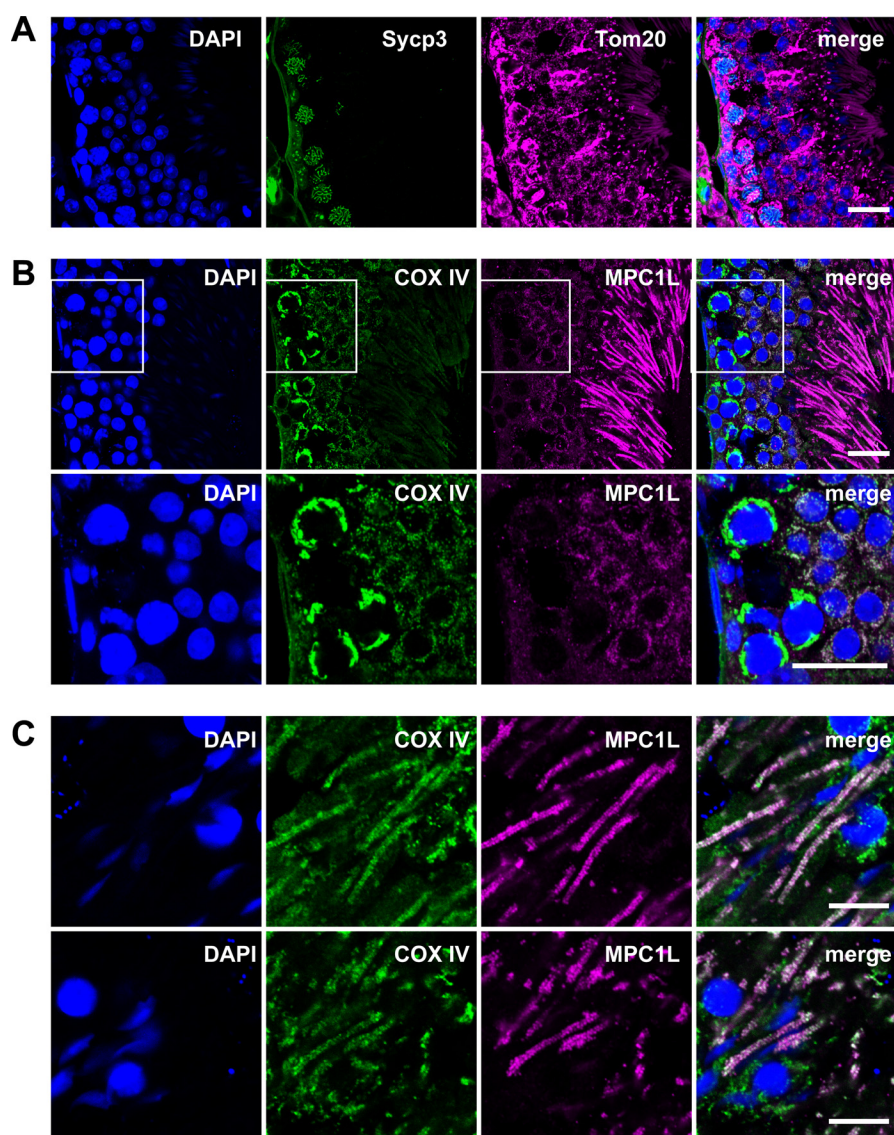
FIGURE 7. **MPC1L is specifically expressed in mitochondria from spermatids and sperm cells.** *A–C,* fluorescent staining of seminiferous tubules from mouse testis. The nuclei were stained with DAPI and immunofluorescent studies were performed using antibodies as follows: Sycp3 and Tom20 (*A*) and complex IV (*CoxIV*) and MPC1L (*B* and *C*). The *lower panel* in *B* shows the *inset* from the *upper panel*. *Scale bars*, 20 μm (*A* and *B*) or 10 μm (*C*).

An evolutionary solution to this problem might be the appearance of the novel *MPC1L* retrogene. Transcription of newly emerged retrogenes is facilitated in spermatids (33), and MPC1L possesses key features of retrogenes, because it is intronless, predicted as a retrotransposed copy by the Retro-Genes track from the UCSC Genome Browser, and encodes a functional protein product (Figs. 3 and 4). In this regard, the localization of the *Mpc1l* gene on the X chromosome is particularly interesting and consistent with the observation that there is a preferred accumulation of male-specific and spermatogenesis genes on this sex chromosome (34–36). This is especially remarkable in the case of *Mpc1l*, the maximal expression of which occurs during the postmeiotic period, when 87% of the genes located on the X chromosome are transcriptionally inactive in mouse males (37). *MPC1L* can thus be added to the group of X chromosome-located, testis-specific, and spermatogenic genes described by Stouffs and Lissens (35). Many of these genes are the subject of a particular focus in the context of male infertility and the specific pattern of MPCL1 expression, suggesting a role in spermiogenesis and/or function of spermatozoa may also implicate MPC1L dysfunction in male infertility.

What could be the importance of MPC1L expression for sperm cell differentiation and/or function? OXPHOS is thought to be crucial for differentiation (2). Postmeiotic male germ cells might benefit from the high potential for MPC activity provided by the elevated MPC1L and MPC2 expression. This could reflect energy substrate availability, because germ cells in the luminal compartment of seminiferous tubules are believed to rely mainly on the breakdown of lactate and pyruvate provided by Sertoli cells (38, 39). Independently of OXPHOS, pyruvate import into mitochondria may serve the anabolic needs of spermiogenesis, for instance for gluconeogenesis that has been suggested to occur in round spermatids in rats (40) or as a source of Acetyl-CoA for histone acetylation (41, 42), a necessary step for the massive compaction of chromatin that occurs during spermiogenesis (43). Development of

reliable *in vitro* models of spermatogenesis will be important in the future to allow the meticulous examination of metabolic fluxes and their role in the various spermatogenic cell types.

Why mitochondrial function is important in sperm cells is not well understood, but it is established that the functionality of this organelle is correlated with sperm quality and fertility (39, 44). A high mitochondrial membrane potential appears correlated with sperm cell motility and fertilization capability (39, 45). However, we did not observe any effect of MPC inhibitors on sperm motility (data not shown), consistent with the consensus view that glycolysis is the main source of energy for flagellar movement despite a possible contribution of OXPHOS. Nevertheless, mitochondria-derived ATP might also be needed for hyperactivation, capacitation, and the acrosome reaction (39, 44); whether the MPC plays any role in these processes remains to be established.

In conclusion, we report the existence in placental mammals of a novel MPC subunit, MPC1L, which is specifically expressed in postmeiotic male germ cells and which has a similar mitochondrial pyruvate import activity compared with the canonical MPC1 subunit. These results provide a more complete picture of the changing composition of the MPC, which is a central node in intermediary metabolism. We also describe for the first time the expression pattern of MPC subunits during spermatogenesis and open the way to further investigation of the physiological relevance of pyruvate metabolism during this process.

Experimental Procedures

Animal Authorizations—Mice were euthanized by CO_2 inhalation. All experimental procedures were performed according to guidelines provided by the Animal Welfare Act and Animal Welfare Ordinance, the Rectors' Conference of the Swiss Universities policy, and the Swiss Academy of Medical Sciences/Swiss Academy of Sciences' Ethical Principles and Guidelines for Experiments on Animals, and were approved by the Geneva Cantonal Veterinary Authority (authorization numbers 1027/3907/1 and GE-40-15).

Antibodies and Reagents—Primary antibodies used in this study were Tom20 (sc-11415; Santa Cruz Biotechnology), MPC1 (HPA045119; Sigma), MPC2 (mouse monoclonal, homemade, available for purchase; AG-20B-0071-C100; AdipoGen Life Sciences), mouse MPC1L (rabbit polyclonal, homemade; Covalab), GFP (11814460001; Roche; cross-reacts with Venus), FLAG M2 (F1804; Sigma), LDHA (3582S; Cell Signaling), mHSP70 (MA3-028; Thermo Scientific), Smac (2409; ProSci), β-tubulin (T4026; Sigma), CoxIV (459600; Thermo Scientific), Sycp3 (97672; Abcam), and SP56 (55101; QED Bioscience). The MPC1L rabbit polyclonal antibody has been generated by four consecutive injections of immunizing peptide and adjuvant. The C-terminal peptide of mouse MPC1L (FLKHQYGGGAK-AKATNPPAK) was used. Immunopurification was performed on a Sepharose column coupled to the antigen. The MPC2 mouse monoclonal antibody was raised against an internal region of MPC2 from human origin (ARPAEKLSTA), that cross-reacts with mouse MPC2. The supernatant from hybridoma cells was desalted on a PD-10 column, and fractions with absorbance at 280 nm were then purified on a protein G-coupled Sepharose column. The specificity of the antibodies

was tested by ELISA and by comparing immunostaining and Western blotting signals in control and mMPC1L-FLAG- and hMPC2-HA-overexpressing cells. Specificity of the mMPC1L antibody was also verified using excess immunizing peptide to block antibody binding during immunofluorescence on mouse testis cryosections. Secondary antibodies were: Alexa 488-, Alexa 594- (Thermo Scientific), or HRP-coupled (Dako) antibodies against rabbit or mouse immunoglobulins. M2 medium was obtained from Sigma-Aldrich.

Molecular Cloning—The MPC1L-Venus and MPC1L-RLuc8 constructs were obtained by assembling the PCR-amplified human MPC1L coding sequence (obtained from HEK293T cells genomic DNA) upstream of the PCR-amplified coding sequences of Venus or RLuc8. Fusion products were inserted between the BamHI/SalI sites of the pWPT vector. All manipulations were performed using Gibson assembly (New England Biolabs). For hMPC1[HA], hMPC1L[HA], and hMPC2[FLAG] constructs, the HA or FLAG tag was added to the C termini during PCR amplification of the corresponding coding sequence (hMPC1L: wild-type coding sequence; hMPC1 and hMPC2: codon optimized coding sequence). The PCR products were then inserted into pRS313 (hMPC1[HA] and hMPC1L[HA]) or pRS316 (hMPC2[FLAG]) using the BamHI and NotI restriction sites for expression under control of the GPD promoter. The mMPC1-FLAG sequence was obtained by adding the FLAG tag sequence downstream of the mouse MPC1 coding sequence by PCR mutagenesis. mMPC1L-FLAG and mMPCLP-FLAG (C-terminal FLAG tag) coding sequences were ordered as gBlocks gene fragments (Integrated DNA Technologies). Inserts containing the mMPC1-FLAG, mMPC1L-FLAG and mMPCLP-FLAG coding sequences were then introduced into the BamHI/SalI sites of pWPT using Gibson assembly. Generation of the MPC1-Venus, MPC2-Venus, MPC2-RLuc8, and matrix or intermembrane space localized Venus (Mx-Venus and IMS-Venus, respectively) encoding constructs were described previously (17). Phusion polymerase (New England Biolabs) was used for all PCRs, and all constructs were sequence-validated (Fasteris).

Isolation of Mitochondria-rich Fraction, Alkali Treatment, Proteinase K Accessibility Test, and Western Blotting—Cell fractionation was performed in MB buffer (210 mM mannitol, 70 mM sucrose, 10 mM HEPES-KOH, pH 7.4, 1 mM EDTA) using a glass homogenizer. Nuclei and cell debris were removed by centrifugation for 5 min at $2,000 \times g$, and a mitochondria-enriched fraction was separated form cytosolic proteins by centrifugation at $13,000 \times g$ for 10 min. For alkali treatment, an aliquot of the mitochondria-rich fraction was treated with 100 mM Na_2CO_3 (pH 11.5) on ice for 20 min. Soluble and integral membrane proteins were separated by ultracentrifugation at $100,000 \times g$ for 30 min. Cytosolic proteins and soluble mitochondrial proteins were submitted to chloroform-methanol precipitation before SDS-PAGE and Western blotting as described elsewhere (25). The proteinase K accessibility test was performed as described previously (46).

Preparation of Lysates from Mouse Tissues and Sperm Cells—Briefly, after dissection, tissues from adult C57bl/6 mouse were rinsed in PBS and then transferred to a prechilled homogenization tube with 300–500 µl of tissue lysis buffer (10 mM Tris, pH

8, 1% Triton X-100, 2 mM EDTA, 13 mM NaCl, protease inhibitor mixture (Roche)). Preset program 5 from the Dispomix Homogenyzer was used for tissue homogenization. The lysate was then spun down 1 min at 1,000 rpm in a microcentrifuge before sonication in a water bath (15 min, 30-s cycles). After 30 min of centrifugation at 13,000 rpm, the supernatant was recovered, and the protein content was quantified using the Bio-Rad protein assay. All steps were performed at 4 °C. SDS sample buffer containing 5% β-mercaptoethanol was added to the samples before separation by SDS-PAGE and transfer to nitrocellulose membranes. For the sperm cell lysates, mouse sperm were obtained by manual trituration of caudae epididymides from adult CD1 mice and allowed to swim in M2 medium for 10 min. After swimming, sperm cells were collected by centrifugation, washed in 1 ml of PBS, resuspended in SDS sample buffer, and boiled for 5 min. Lysates were centrifuged, 5% β-mercaptoethanol was added to the supernatants, and the mixture was boiled again for 5 min prior to analysis by SDS-PAGE.

Cell Culture and Viral Production—All cultured cells were mycoplasma-free. Generation of immortalized MPC1 KO MEFs was described previously (25). HEK293T, HeLa, and MEFs cell lines were cultured in DMEM containing 4.5 g/liter glucose, 2 mM glutamine, 10% FBS, and 1% penicillin/streptomycin (Invitrogen). For lentiviral particle production, pWPT plasmid containing the sequence of interest was co-transfected with the viral plasmids psPAX2 and pMD2G (Addgene) into HEK293T cells. After 48 h, the supernatant was collected, centrifuged at 3,000 rpm for 5 min, filtered (polyethersulfone glass, 0.45-μm pores), and used to infect HeLa cells or MPC1 KO MEFs.

Yeast Strains and Culture—Generation of the *mpc1Δ/ mpc2Δ/mpc3Δ* strain (MAT**a** *ura3Δ0 his3Δ1 mpc1::KanR mpc2::hph mpc3::NatR*) from the wild-type RL285–16C requiring uracil and histidine (his ura) was described previously (7). This strain was co-transformed with two plasmids (pRS313 and pRS316), either empty or expressing the indicated MPC subunits, and cultured in SD medium containing all amino acids except histidine and uracil, which were omitted for plasmid maintenance. Where indicated, the branched chain amino acids leucine and valine were also omitted. For spot assays, overnight cultures of the indicated strains were grown in the appropriate medium and diluted to an A_{600} of 0.2. Serial 5-fold dilutions were spotted on plates with the appropriate medium and grown for 2 days at 30 °C.

Bioluminescence Resonance Energy Transfer (BRET) Analysis—BRET kinetic experiments were performed as previously described (17) in HEK293T cells transfected 48 h prior to the experiment with MPC1L-RLuc8 + MPC2-Venus, MPC2-RLuc8 + MPC1L-Venus, or MPC2-RLuc8 + MPC1-Venus. The cells seeded in 96-well plates (Greiner Bio-One, Ref. 655098) were washed with PBS (supplemented with 1 mM $CaCl_2$ and 0.5 mM $MgCl_2$), and measurements were performed 5 min after addition of 5 mM coelenterazine h substrate (Invitrogen). Two filter settings were used for signal detection (RLuc8 filter, 460 ± 40 nm; and Venus filter, 528 ± 20 nm) at 37 °C using the Synergy 2 plate reader (Biotek). The BRET value was defined as the difference between the emission at 528 nm/460 nm of co-transfected RLuc8 and Venus MPC fusion proteins and the emission at 528 nm/460 nm of the RLuc8

fusion alone (MPC2-RLuc8 or MPC1L-RLuc8). Where indicated, PBS, pyruvate (5 mM), or UK5099 (10 μM) was injected in the wells. For spectral scanning, 5 min after addition of 5 mM coelenterazine h, the luminescence intensity was measured every 2 nm from 350 to 650 nm at 37 °C using the Synergy 2 plate reader equipped with a monochromator.

Oxygen Consumption—Oxygen consumption rate in MEFs permeabilized with 1 nM XF-PMP was measured using the Seahorse XF^{e}24 Flux Analyzer (Seahorse Biosciences) as described previously (25). Variable pyruvate concentrations were used for the experiment shown in Fig. 4*A*.

Pyruvate Decarboxylation Assay—Pyruvate decarboxylation assay was performed essentially as described elsewhere (47). A piece of chromatography paper (0.6 × 1 cm) was put on top of microbridges (Hampton Research) fitted in wells of a 24-well plate. The assay medium was composed of DMEM containing 10% FCS, 4 mM glutamine, and 6 mM sodium pyruvate supplemented with 0.3 μCi/ml of [1-^{14}C]pyruvate (PerkinElmer). To remove any $^{14}CO_2$ produced from spontaneous decarboxylation, the assay medium was warmed to 37 °C for 2 h, and then an aliquot was used to quantify radioactivity in a scintillation counter. This allowed us to determine the specific activity of pyruvate (assuming a pyruvate concentration of 6 mM), which ranged from 60 to 100 CPM/nmol pyruvate. 1 million cells/well were suspended in 350 μl of assay medium on ice, and each chromatography paper was moistened with 30 μl of 2 N NaOH. After sealing the plate with adhesive film to avoid contamination of $^{14}CO_2$ between wells, the plate was placed in a 37 °C water bath to start pyruvate metabolism. 15 min later, 50 μl of 20% trichloroacetic acid was added to each cell suspension to terminate metabolism. After resealing, the plate was put back at 37 °C for 1 h to allow complete release of $^{14}CO_2$. Chromatography papers containing $^{14}CO_2$ were then collected for scintillation counting. Pyruvate oxidation rates (expressed as nmol/10^6 cells/h) were extrapolated from the total specific activity in the reaction. Background levels of $^{14}CO_2$ were obtained from wells containing assay medium without cells and subtracted from the values obtained from cell-containing wells.

Immunofluorescence—For immunofluorescence using HeLa cells, the cells were grown on glass coverslips and fixed in 4% paraformaldehyde with 4% sucrose in PBS for 10 min. After permeabilization in 0.15% Triton X-100 for 5 min and blocking in 5% normal goat serum for 30 min, the cells were incubated with primary antibody for 2 h, rinsed in PBS, and incubated with secondary antibody for 1 h. The nuclei were stained with DAPI, and the coverslips were mounted on microscope slides. All steps were performed at room temperature. For immunofluorescence on mouse testis sections, testes from adult CD1 mice were fixed overnight in 4% paraformaldehyde in PBS and cryoprotected in 20% sucrose in PBS for at least 48 h. 10-μm cryosections were placed on SuperFrost Plus glass slides, dried, and conserved at −80 °C. Cryosections were then thawed, rehydrated in PBS, and heat-mediated antigen retrieval was performed in citrate buffer (0.01 M sodium citrate, pH 6). After 20 min of permeabilization in 0.1% Triton X-100 in PBS, nonspecific sites were blocked by incubation for 30 min in blocking buffer (3% bovine serum albumin, 0.1% Tween 20 in PBS) before primary antibody incubation overnight at 4 °C in block-

ing buffer. After rinsing and secondary antibody incubation for 1 h at room temperature, sections were counterstained with DAPI and mounted in glycerol mounting medium. Fluorescence images were captured with a Zeiss LSM700 confocal microscope equipped with a 63× oil objective. Z-stack images (0.2- or 0.4-μm steps for cultured cells or sections, respectively) were acquired, before image processing (including uniform contrast enhancement) and creation of stack projections using the Fiji software (based on ImageJ).

Trypan Blue Quenching Experiment—HeLa cells plated in MatTek 35-mm glass-bottomed dishes were treated for 1 min with 50 μM digitonin in intracellular buffer (130 mM KCl, 10 mM NaCl, 2 mM K_2HPO_4, 1 mM $MgCl_2$, 20 mM HEPES, pH 7, at 37 °C) to permeabilize the plasma membrane and the outer mitochondrial membrane. After rinsing, Z-stack images (0.5-μm steps) of the cells were obtained every 30 s with a spinning disc confocal microscope, before and after addition of 0.01% trypan blue. For each cell and for each time point, fluorescence intensity in the best focus image was measured using the ImageJ software. The remaining fluorescence after addition of trypan blue was calculated and expressed as a fraction of the remaining fluorescence in the Mx-Venus condition. Live cells imaging was performed with a spinning disc confocal system (Intelligent Imaging Innovations Marianas SDC) mounted on an inverted microscope (Leica DMIRE2), equipped with a 63× glycerin objective and an emCCD Evolve 512 camera (Photometrics).

Sequence Alignments and Statistical Analysis—Pairwise sequence alignments were performed using EMBOSS Needle, and multiple sequence alignments were performed using ClustalOmega. Jalview was used for formatting the sequence alignments with the Clustal X color setting. Unpaired *t* test was used to analyze the data from trypan blue quenching experiments. For the oxygen consumption and pyruvate decarboxylation experiments, one-way analysis of variance was performed. All statistical analyses were done using the GraphPad PRISM software.

References

1. Vander Heiden, M. G., Cantley, L. C., and Thompson, C. B. (2009) Understanding the Warburg effect: the metabolic requirements of cell proliferation. *Science* **324,** 1029–1033
2. Folmes, C. D., Dzeja, P. P., Nelson, T. J., and Terzic, A. (2012) Metabolic plasticity in stem cell homeostasis and differentiation. *Cell Stem Cell* **11,** 596–606
3. Agathocleous, M., Love, N. K., Randlett, O., Harris, J. J., Liu, J., Murray, A. J., and Harris, W. A. (2012) Metabolic differentiation in the embryonic retina. *Nat. Cell Biol.* **14,** 859–864
4. Agathocleous, M., and Harris, W. A. (2013) Metabolism in physiological cell proliferation and differentiation. *Trends Cell Biol.* **23,** 484–492
5. Hanahan, D., and Weinberg, R. A. (2011) Hallmarks of cancer: the next generation. *Cell* **144,** 646–674
6. Palmieri, F., Pierri, C. L., De Grassi, A., Nunes-Nesi, A., and Fernie, A. R. (2011) Evolution, structure and function of mitochondrial carriers: a review with new insights. *Plant J.* **66,** 161–181
7. Herzig, S., Raemy, E., Montessuit, S., Veuthey, J.-L., Zamboni, N., Westermann, B., Kunji, E. R., and Martinou, J.-C. (2012) Identification and functional expression of the mitochondrial pyruvate carrier. *Science* **337,** 93–96
8. Bricker, D. K., Taylor, E. B., Schell, J. C., Orsak, T., Boutron, A., Chen, Y.-C., Cox, J. E., Cardon, C. M., Van Vranken, J. G., Dephoure, N., Redin, C., Boudina, S., Gygi, S. P., Brivet, M., Thummel, C. S., *et al.* (2012) A mitochondrial pyruvate carrier required for pyruvate uptake in yeast, Drosophila, and humans. *Science* **337,** 96–100
9. Schell, J. C., and Rutter, J. (2013) The long and winding road to the mitochondrial pyruvate carrier. *Cancer Metab.* **1,** 6
10. Bender, T., Pena, G., and Martinou, J.-C. (2015) Regulation of mitochondrial pyruvate uptake by alternative pyruvate carrier complexes. *EMBO J.* **34,** 911–924
11. Patterson, J. N., Cousteils, K., Lou, J. W., Manning Fox, J. E., MacDonald, P. E., and Joseph, J. W. (2014) Mitochondrial metabolism of pyruvate is essential for regulating glucose-stimulated insulin secretion. *J. Biol. Chem.* **289,** 13335–13346
12. Vigueira, P. A., McCommis, K. S., Schweitzer, G. G., Remedi, M. S., Chambers, K. T., Fu, X., McDonald, W. G., Cole, S. L., Colca, J. R., Kletzien, R. F., Burgess, S. C., and Finck, B. N. (2014) Mitochondrial pyruvate carrier 2 hypomorphism in mice leads to defects in glucose-stimulated insulin secretion. *Cell Rep.* **7,** 2042–2053
13. Gray, L. R., Sultana, M. R., Rauckhorst, A. J., Oonthonpan, L., Tompkins, S. C., Sharma, A., Fu, X., Miao, R., Pewa, A. D., Brown, K. S., Lane, E. E., Dohlman, A., Zepeda-Orozco, D., Xie, J., Rutter, J., *et al.* (2015) Hepatic mitochondrial pyruvate carrier 1 is required for efficient regulation of gluconeogenesis and whole-body glucose homeostasis. *Cell Metab.* **22,** 669–681
14. McCommis, K. S., Chen, Z., Fu, X., McDonald, W. G., Colca, J. R., Kletzien, R. F., Burgess, S. C., and Finck, B. N. (2015) Loss of mitochondrial pyruvate carrier 2 in the liver leads to defects in gluconeogenesis and compensation via pyruvate-alanine cycling. *Cell Metab.* **22,** 682–694
15. Schell, J. C., Olson, K. A., Jiang, L., Hawkins, A. J., Van Vranken, J. G., Xie, J., Egnatchik, R. A., Earl, E. G., DeBerardinis, R. J., and Rutter, J. (2014) A role for the mitochondrial pyruvate carrier as a repressor of the Warburg effect and colon cancer cell growth. *Mol. Cell* **56,** 400–413
16. Wang, L., Xu, M., Qin, J., Lin, S.-C., Lee, H.-J., Tsai, S. Y., and Tsai, M.-J. (2016) MPC1, a key gene in cancer metabolism, is regulated by COUPTFII in human prostate cancer. *Oncotarget* **7,** 14673–14683
17. Compan, V., Pierredon, S., Vanderperre, B., Krznar, P., Marchiq, I., Zamboni, N., Pouyssegur, J., and Martinou, J.-C. (2015) Monitoring mitochondrial pyruvate carrier activity in real time using a BRET-based biosensor: investigation of the Warburg effect. *Mol. Cell* **59,** 491–501
18. Eboli, M. L., Paradies, G., Galeotti, T., and Papa, S. (1977) Pyruvate transport in tumour-cell mitochondria. *Biochim. Biophys. Acta* **460,** 183–187
19. Paradies, G., Capuano, F., Palombini, G., Galeotti, T., and Papa, S. (1983) Transport of pyruvate in mitochondria from different tumor cells. *Cancer Res.* **43,** 5068–5071
20. Zhong, Y., Li, X., Yu, D., Li, X., Li, Y., Long, Y., Yuan, Y., Ji, Z., Zhang, M.,

Wen, J.-G., Nesland, J. M., Suo, Z., Zhong, Y., Li, X., Yu, D., *et al.* (2015) Application of mitochondrial pyruvate carrier blocker UK5099 creates metabolic reprogram and greater stem-like properties in LnCap prostate cancer cells in vitro. *Oncotarget* **6,** 37758–37769

21. Liang, L., Li, Q., Huang, L., Li, D., and Li, X. (2015) Sirt3 binds to and deacetylates mitochondrial pyruvate carrier 1 to enhance its activity. *Biochem. Biophys. Res. Commun.* **468,** 807–812

22. Krogh, A., Larsson, B., von Heijne, G., and Sonnhammer, E. L. (2001) Predicting transmembrane protein topology with a hidden Markov model: application to complete genomes. *J. Mol. Biol.* **305,** 567–580

23. Giacomello, M., Drago, I., Bortolozzi, M., Scorzeto, M., Gianelle, A., Pizzo, P., and Pozzan, T. (2010) Ca^{2+} hot spots on the mitochondrial surface are generated by Ca^{2+} mobilization from stores, but not by activation of store-operated Ca^{2+} channels. *Mol. Cell* **38,** 280–290

24. De Stefani, D., Raffaello, A., Teardo, E., Szabò, I., and Rizzuto, R. (2011) A forty-kilodalton protein of the inner membrane is the mitochondrial calcium uniporter. *Nature* **476,** 336–340

25. Vanderperre, B., Herzig, S., Krznar, P., Hörl, M., Ammar, Z., Montessuit, S., Pierredon, S., Zamboni, N., and Martinou, J.-C. (2016) Embryonic lethality of mitochondrial pyruvate carrier 1 deficient mouse can be rescued by a ketogenic diet. *PLoS Genet.* **12,** e1006056

26. San Martín, A., Ceballo, S., Baeza-Lehnert, F., Lerchundi, R., Valdebenito, R., Contreras-Baeza, Y., Alegría, K., and Barros, L. F. (2014) Imaging mitochondrial flux in single cells with a FRET sensor for pyruvate. *PLoS One* **9,** e85780

27. Marchiq, I., Le Floch, R., Roux, D., Simon, M.-P., and Pouyssegur, J. (2015) Genetic disruption of lactate/H+ symporters (MCTs) and their subunit CD147/BASIGIN sensitizes glycolytic tumor cells to phenformin. *Cancer Res.* **75,** 171–180

28. Kim, M.-S., Pinto, S. M., Getnet, D., Nirujogi, R. S., Manda, S. S., Chaerkady, R., Madugundu, A. K., Kelkar, D. S., Isserlin, R., Jain, S., Thomas, J. K., Muthusamy, B., Leal-Rojas, P., Kumar, P., Sahasrabuddhe, N. A., *et al.* (2014) A draft map of the human proteome. *Nature* **509,** 575–581

29. Pagliarini, D. J., Calvo, S. E., Chang, B., Sheth, S. A., Vafai, S. B., Ong, S.-E., Walford, G. A., Sugiana, C., Boneh, A., Chen, W. K., Hill, D. E., Vidal, M., Evans, J. G., Thorburn, D. R., Carr, S. A., *et al.* (2008) A mitochondrial protein compendium elucidates complex I disease biology. *Cell* **134,** 112–123

30. Gan, H., Wen, L., Liao, S., Lin, X., Ma, T., Liu, J., Song, C.-X., Wang, M., He, C., Han, C., and Tang, F. (2013) Dynamics of 5-hydroxymethylcytosine during mouse spermatogenesis. *Nat. Commun.* **4,** 1995

31. Parra, M. T., Viera, A., Gómez, R., Page, J., Carmena, M., Earnshaw, W. C., Rufas, J. S., and Suja, J. A. (2003) Dynamic relocalization of the chromosomal passenger complex proteins inner centromere protein (INCENP) and aurora-B kinase during male mouse meiosis. *J. Cell Sci.* **116,** 961–974

32. Kim, K. S., Cha, M. C., and Gerton, G. L. (2001) Mouse sperm protein sp56 is a component of the acrosomal matrix. *Biol. Reprod.* **64,** 36–43

33. Soumillon, M., Necsulea, A., Weier, M., Brawand, D., Zhang, X., Gu, H., Barthès, P., Kokkinaki, M., Nef, S., Gnirke, A., Dym, M., de Massy, B., Mikkelsen, T. S., and Kaessmann, H. (2013) Cellular source and mechanisms of high transcriptome complexity in the mammalian testis. *Cell Rep.* **3,** 2179–2190

34. Lercher, M. J., Urrutia, A. O., and Hurst, L. D. (2003) Evidence that the human X chromosome is enriched for male-specific but not female-specific genes. *Mol. Biol. Evol.* **20,** 1113–1116

35. Stouffs, K., and Lissens, W. (2012) X chromosomal mutations and spermatogenic failure. *Biochim. Biophys. Acta* **1822,** 1864–1872

36. Rice, W. R. (1984) Sex chromosomes and the evolution of sexual dimorphism. *Evolution* **38,** 735–742

37. Namekawa, S. H., Park, P. J., Zhang, L.-F., Shima, J. E., McCarrey, J. R., Griswold, M. D., and Lee, J. T. (2006) Postmeiotic sex chromatin in the male germline of mice. *Curr. Biol. CB.* **16,** 660–667

38. Rato, L., Alves, M. G., Socorro, S., Duarte, A. I., Cavaco, J. E., and Oliveira, P. F. (2012) Metabolic regulation is important for spermatogenesis. *Nat. Rev. Urol.* **9,** 330–338

39. Ramalho-Santos, J., Varum, S., Amaral, S., Mota, P. C., Sousa, A. P., and Amaral, A. (2009) Mitochondrial functionality in reproduction: from gonads and gametes to embryos and embryonic stem cells. *Hum. Reprod Update* **15,** 553–572

40. Yáñez, A. J., Bustamante, X., Bertinat, R., Werner, E., Rauch, M. C., Concha, I. I., Reyes, J. G., and Slebe, J. C. (2007) Expression of key substrate cycle enzymes in rat spermatogenic cells: fructose 1,6 bisphosphatase and 6 phosphofructose 1-kinase. *J. Cell Physiol.* **212,** 807–816

41. Choudhary, C., Weinert, B. T., Nishida, Y., Verdin, E., and Mann, M. (2014) The growing landscape of lysine acetylation links metabolism and cell signalling. *Nat. Rev. Mol. Cell Biol.* **15,** 536–550

42. Galdieri, L., Zhang, T., Rogerson, D., Lleshi, R., and Vancura, A. (2014) Protein acetylation and acetyl coenzyme a metabolism in budding yeast. *Eukaryot. Cell* **13,** 1472–1483

43. Qian, M.-X., Pang, Y., Liu, C. H., Haratake, K., Du, B.-Y., Ji, D.-Y., Wang, G.-F., Zhu, Q.-Q., Song, W., Yu, Y., Zhang, X.-X., Huang, H.-T., Miao, S., Chen, L.-B., Zhang, Z.-H., (2013) Acetylation-mediated proteasomal degradation of core histones during DNA repair and spermatogenesis. *Cell* **153,** 1012–1024

44. Amaral, A., Lourenço, B., Marques, M., and Ramalho-Santos, J. (2013) Mitochondria functionality and sperm quality. *Reproduction* **146,** R163–R174

45. Gallon, F., Marchetti, C., Jouy, N., and Marchetti, P. (2006) The functionality of mitochondria differentiates human spermatozoa with high and low fertilizing capability. *Fertil. Steril.* **86,** 1526–1530

46. Jourdain, A. A., Koppen, M., Wydro, M., Rodley, C. D., Lightowlers, R. N., Chrzanowska-Lightowlers, Z. M., and Martinou, J.-C. (2013) GRSF1 regulates RNA processing in mitochondrial RNA granules. *Cell Metab.* **17,** 399–410

47. Yang, C., Harrison, C., Jin, E. S., Chuang, D. T., Sherry, A. D., Malloy, C. R., Merritt, M. E., and DeBerardinis, R. J. (2014) Simultaneous steady-state and dynamic 13C NMR can differentiate alternative routes of pyruvate metabolism in living cancer cells. *J. Biol. Chem.* **289,** 6212–6224